Title
The concept of delayed nucleation in nanocrystal growth demonstrated for the case of iron oxide nanodisks

Permalink
https://escholarship.org/uc/item/5qq8n3fz

Authors
Casula, Maria F.
Jun, Young-wook
Zaziski, David J.
et al.

Publication Date
2005-09-09

Peer reviewed

The concept of Delayed Nucleation in nanocrystal growth demonstrated for the case of Iron Oxide Nanodisks

Maria F. Casula[1, 2]*, Young-wook Jun[1,3], David J. Zaziski[1,4], Emory M. Chan[1,5], Anna Corrias[2] and A. Paul Alivisatos[1,5]*

[1]Department of Chemistry, University of California at Berkeley, Berkeley, CA 94720, USA

[2]Dipartimento di Scienze Chimiche, University of Cagliari, Italy, I-09042

[3] Present address: Department of Chemistry, Yonsei University, Seoul 120-749, Korea

[4] Present address: Nanosys, Inc., 2625 Hanover Street, Palo Alto, CA 94304, USA.

[5] Division of Materials Science, Lawrence Berkeley National Laboratory, Berkeley, CA 94720, USA

casulaf@unica.it; alivis@uclink4.berkeley.edu

RECEIVED DATE (to be automatically inserted after your manuscript is accepted if required according to the journal that you are submitting your paper to)

TITLE RUNNING HEAD. Monodisperse Iron Oxide Nanodisks by Delayed Nucleation

ABSTRACT

A comprehensive study of iron oxide nanocrystal growth through non-hydrolitic, surfactant-mediated thermal reaction of iron pentacarbonyl and an oxidizer has been conducted, which includes size control, anisotropic shape evolution, and crystallographic phase transition of monodisperse iron oxide colloidal nanocrystals. The reaction was monitored by *in situ* UV-Vis spectroscopy taking advantage of the color change accompanying the iron oxide colloid formation allowing measurement of the induction time for nucleation. Features of the synthesis such as the size control and reproducibility are related to the occurrence of the observed delayed nucleation process. As a separate source of iron and oxygen is adopted, phase control could also be achieved by sequential injections of oxidizer.

Introduction

Methods for the synthesis of monodisperse nanostructures are of key importance in inorganic and physical chemistry. For instance, it allows one to interpret the collective physical properties of an ensemble of particles in terms of the features of an individual particle.[1] Monodisperse particles are also an important requirement for the application of nanoparticles in a wide variety of materials.

Recently, many efforts have been focused on developing synthesis procedures aiming at controlling nucleation and growth of monodisperse nanoparticles[2-6], which play a key role in determining the crystal size distribution. In particular, a successful scheme relies on the separation of the nucleation from the growth which can be obtained by producing a single fast nucleation event induced by injecting thermally unstable precursors into a hot solution containing surfactants, followed by a surfactant-mediated growth.[7] By adsorbing reversibly to nanoparticle surfaces, surfactants provide a means not only of mediating growth but also of stabilizing the nanoparticles in solution. For this reason this approach has been extensively adopted for the preparation of colloidal nanoparticles which have provided model systems for the study of crystal growth and of factors affecting phase and shape stability at the nanometer scale. [8-13]

Many recent studies point out the effect of the growth conditions on the outcome of the synthesis: for example by varying the growth temperature one may achieve size and/or shape control by tuning the growth rate or phase control by making more favorable the growth of one polymorph. On the other hand, the nucleation is more difficult to control as it depends exponentially on concentration and temperature. Rapid injection leads to a burst of nucleation, but also creates a complex sequence of events than can be difficult to reproduce. For instance, just after injection volatile by-products evolve, the temperature and the concentration may not be uniform until complete mixing, and the exo- or endo-thermicity of the reactions also make transient changes in the conditions. Techniques such as size distribution focusing can be used to compensate for the variations in nucleation conditions. However, here we demonstrate a more robust method for creating reproducible nucleation, using the concept of delayed nucleation. In delayed nucleation, the initial precursor is slowly converted subsequent to

injection to an active species. When the concentration of the active species builds up and then exceeds the nucleation threshold, a brief period of nucleation ensues. We illustrate this concept using the synthesis of iron oxide nanocrystals from an iron pentacarbonyl precursor. This system is chosen because the formation of iron oxide nanocrystals is generally well established, and because thermal decomposition of iron pentacarbonyl is very well documented.

This system is also of interest, because the rich phase diagram of the iron oxides represent a class of extremely relevant materials not only in chemistry but also in areas such as magnetism[14], soil science[15], catalysis[16], and more recently medicine[17] and energetic materials[18,19]. A non-hydrolitic preparation of iron oxide crystals is appealing in that in principle it allows one to achieve a dependable synthetic procedure by avoiding the complex aqueous chemistry[20]. For this reason, the preparation of iron oxide nanoparticles by non-hydrolytic methods has been recently proposed which make use of either single molecular precursor systems such as Fe-Cup and Fe(acac)$_3$, and Fe(oleate)$_3$ complexes[21-26] or dual source systems[27,28]. Although high quality iron oxide nanocrystals with different sizes are produced by these routes, further improvement in phase and shape control is still desirable.

In this work, we synthesize iron oxide nanocrystals through the co-injection of iron pentacarbonyl and an oxidizer, *m*-chloroperoxybenzoic acid, into hot organic solvent containing fatty acid surfactants. This system enables not only the systematic monitoring of the nanocrystal formation in terms of nucleation, crystalline phase, and size but also of anisotropic nanocrystal growth. Specifically, we describe (i) the size evolution depending on growth time and temperature, (ii) crystalline phase transition during the nanocrystal growth and the effect of oxidants on the final crystalline phase, (iii) the formation and characterization of disk shaped nanocrystals, and (iv) direct evidence of nanocrystal nucleation processes by *in situ* optical monitoring. Unlike conventional precursor injection methods, we observe that iron oxide nanocrystal growth is promoted by the sudden occurrence of a nucleation delayed in time. This sudden delayed nucleation is highly related to the homogeneous nucleation and the kinetic growth of nanocrystals, which ultimately results in the formation of monodisperse iron oxide nanodisks.

Experimental Section

Materials The synthesis was carried out using standard airless procedures and commercially available reagents. Iron Pentacarbonyl ($Fe(CO)_5$, 99.5%) and tridecanoic acid ($C_{13}H_{26}O_2$, 98%) were purchased from Alfa Aesar and Aldrich, respectively, and were used without further purification. 3-chloro peroxybenzoic acid (or meta-chloro peroxybenzoic acid, mCPBA) ($C_7H_5O_2Cl$, 77% Aldrich) was dehydrated with a procedure including extraction with dichloromethane and dehydration with phosphorous anhydride, followed by vacuum drying. Dioctylether ($C_{16}H_{34}O$, 99%, Aldrich) was used as solvent.

Iron oxide nanocrystal synthesis In a typical synthesis, a solution of tridecanoic acid in octyl ether in a 25 mL 3-necked flask connected to a Liebig condenser was outgassed for 30 minutes and then heated under Ar flow at 293 ºC. A solution of iron pentacarbonyl in ether and a solution of mCPBA in ether were then rapidly co-injected. Unless otherwise stated, the iron molar concentration was 0.1 M, and the iron:surfactant:oxidizer molar ratios were 1:3:1.5. The solution flask was heated at 293 °C for 5 minutes to allow particle growth, after which time the solution was cooled to 40 °C, and ethanol was added to precipitate nanoparticles from the solution. The particles were separated by centrifugation and washed twice by redispersing in toluene and precipitating with ethanol. Due to the monodispersity of the nanoparticles, no further size selection procedure was carried out on any samples. This reaction was found to be highly reproducible.

Effect of secondary injection of oxidizer One minute after the solution turns dark, an ether solution of mCPBA was injected at 293 °C. The amount of oxidizer injected was varied from 0.5 to 1.5 times the moles of iron pentacarbonyl. After a growth time of 4 minutes at 293 °C the solution was cooled down and the nanoparticles were precipitated from the solution by adding ethanol.

In situ UV-Vis monitoring of Fe_3O_4 nanocrystal growth To monitor the progress of the reaction, UV-Visible absorption spectra of the solution were collected in situ using a stainless steel dip probe (Ocean Optics) with a 5 mm path length. The dip probe was connected via a 300 μm fiber optics to an Ocean

Optics USB2000 CCD spectrometer, and a custom LabView program recorded absorption spectra and temperatures at 5 s intervals. Nanocrystal evolution was analyzed by plotting the baseline-corrected absorption at selected wavelengths versus time.

Characterization The nanocrystals were characterized by conventional and high resolution transmission electron microscopy (TEM and HR-TEM), X-Ray powder diffraction (XRD), Raman spectroscopy and atomic force microscopy (AFM). TEM analysis was performed at the Electron Microscopy Laboratory (EML) at the University of California, Berkeley, on a FEI Tecnai 12 using an operating voltage of 100kV. Nanocrystals were deposited from toluene solution onto 200 mesh formvar coated copper grids (purchased from Ted Pella) and dried in air. TEM statistical analyses were performed on at least 500 particles. HRTEM observations were performed on a Hitachi H9000-NAR operating at an accelerating voltage of 300 kV. X-ray diffraction was performed on a Bruker-AXS D8 general area detector diffraction system (GADDS), using Co Kα radiation (1.79026 Å). Two-dimensional patterns were angle integrated to obtain the patterns displayed. The instrument resolution is 0.07º in 2θ and the accumulation time for each frame of each sample was 40 minutes. Two frames were taken per sample, centered at 2θ angles of 40º and 60º, and at Ω angles of 20º and 35º respectively. Raman spectra were collected on the powdered iron oxide samples using a confocal micro-Raman setup. All spectra were excited using laser powers <0.5 mW (spot size ~20 um) of the 633 nm line of a 40 mW aircooled HeNe laser in order to avoid sample decomposition or temperature induced phase transformations such as $Fe_3O_4 \rightarrow \gamma\text{-}Fe_2O_3$, and $\gamma\text{-}Fe_2O_3 \rightarrow \alpha\text{-}Fe_2O_3$.[29] The scattered light was collected in a backscattering geometry and spectral dispersion was accomplished using a ¾ meter grating monochromator with a 1200 grooves·mm^{-1} grating blazed at 700 nm yielding a final resolution of <1cm^{-1}. The Raman spectra were recorded with a liquid nitrogen cooled CCD camera. Confocal spatial filtering was accomplished using the entrance slit of the monochromator and electronic aperturing of the detector. Acquisition times were 30 minutes. Calibration of the absolute frequency was done using a neon pen lamp. Reference bulk iron oxides were obtained from Aldrich and used as received.

Nanocrystal shape evaluation AFM analysis was performed on a Digital Instrument Nanoscope IIIa Multimode Atomic Force Miscoscope. The sample was prepared by depositing a few drops of a dilute toluene solution of the nanoparticles onto a highly ordered pyrolytic graphite support (purchased from SPI Supplies) by spin coating (spinning rate 4000 rpm). Images were processed by the instrument's software. The images were flattened to remove the background slope, taking care of excluding the particles from the flattened area, and the section analysis on the flattened images provided the particle height. The height was calibrated from graphite terrace standards.

Results

Nanocrystal size and size evolution with growth time

Figure 1 shows the TEM image of the iron oxide sample obtained adopting $Fe(CO)_5$:tridecanoic acid:mCPBA ratio of 1:3:1.5. The low magnification shows a 2D-monolayer of nearly monodisperse nanoparticles. The inset shows that the sample presents faceted nanoparticles with average diameter of 13 nm.

Figure 2 shows the size-evolution profile as a function of the growth time as obtained by TEM analysis. The diameter of the nanoparticles increases rapidly with time and the increase in the particle average diameter is accompanied by a broadening of the size distribution. [30]
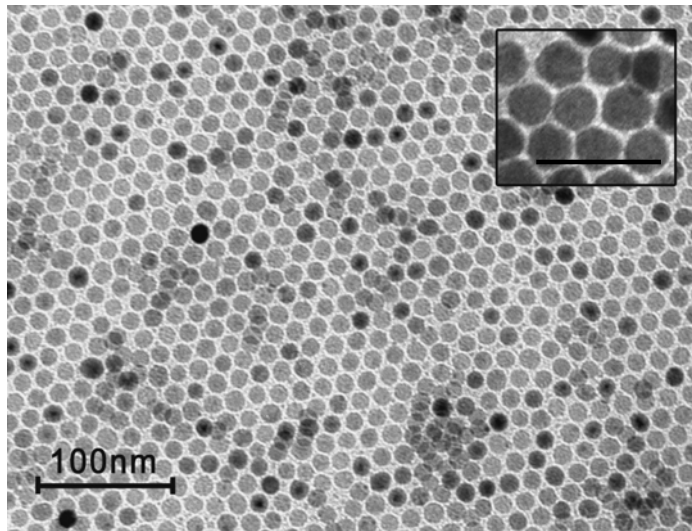
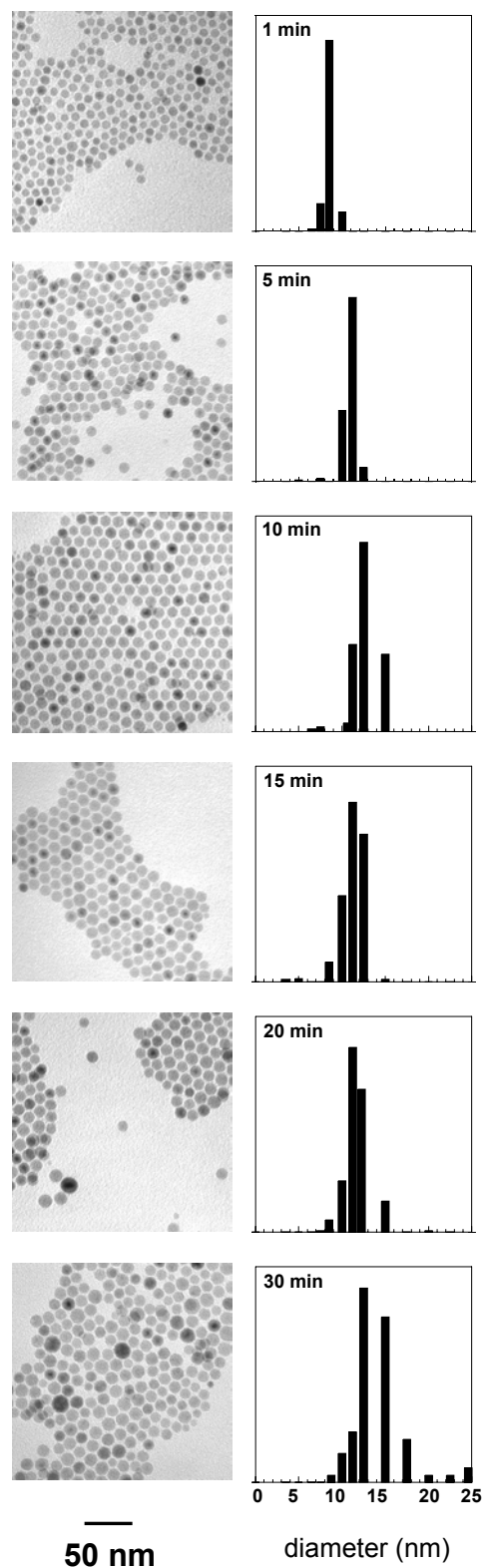**Figure 1.** TEM image of iron oxide nanocrystals obtained by using a Fe(CO)$_5$:mCPBA=1:1.5. Scale bar in the inset is 50 nm.

Figure 2. TEM images (left) and size distributions (right) obtained by using a Fe(CO)$_5$:mCPBA=1:1.5 at increasing growth time.

Nanocrystal shape determination

In the sample obtained after a growth time of 5 minutes individual nanoparticles, and self-assembled monolayers and multilayers are imaged depending on the deposition conditions. The typical AFM image of isolated particles and the surface plot of the self-assemblies are reported in Figure 3A and 3B respectively. The section analysis was performed in order to measure the height of the nanoparticles, h_i, and of the self-assembled assemblies h_a; in particular the assemblies made out of three layers were considered (see Supplementary Information). The height of individual nanoparticles and of the three monolayers as obtained by statistical section analysis is 3.16 nm and 14.66 nm, respectively (see Supporting Information). On the other hand, the width of the nanoparticles is not resolved due to the convolution of the tip, as expected.
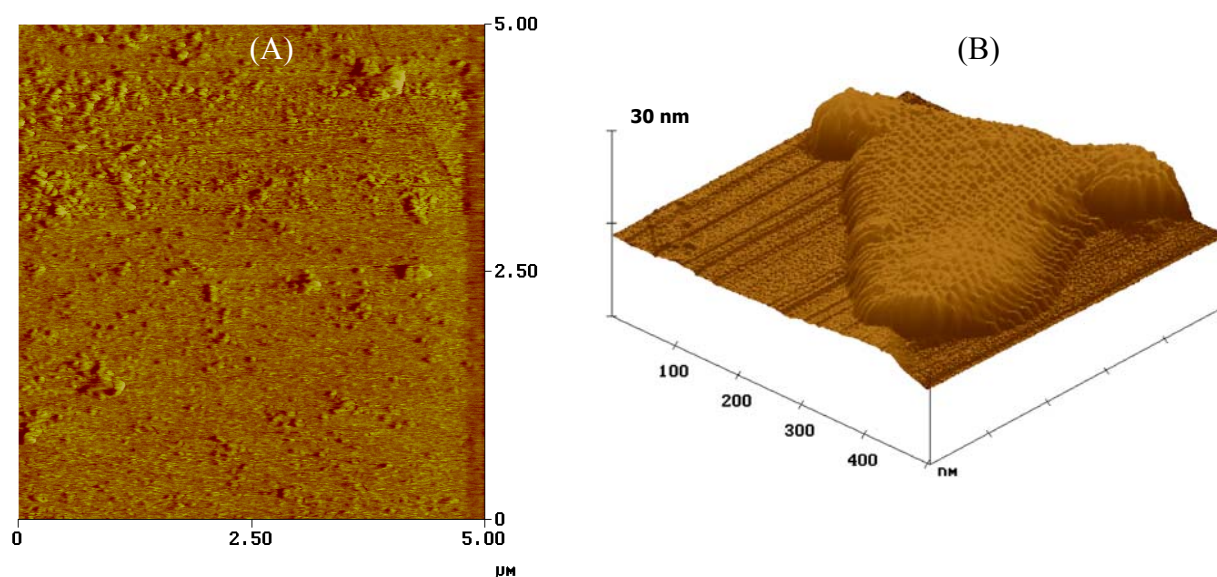

Figure 3. AFM image of iron oxide nanocrystals obtained by using a Fe(CO)$_5$:mCPBA=1:1.5, isolated particles (A) and a 3D representation of an AFM image of a self-assembled multilayer (B).

Real-time UV-Visible measurements of the reactant solution

Under the reported conditions, when the solution of iron pentacarbonyl (yellow-orange) and the solution of mCPBA (colorless) are co-injected, the solution quickly turns from pale yellow to dark brown for less than a 1 minute, then turns back to yellow and a vigorous release of white vapors is observed. After about 1 hour, the solution suddenly turns dark, coincident with the formation of the

colloid.[31,32] This reaction mechanism is very reproducible, and no particles can be isolated from the solution until the solution turns dark. We have made use of in situ absorption spectroscopy in order to gain information on the formation of iron oxide nanocrystals in situ. Absorption spectroscopy has already shown to be a powerful tool for investigating nucleation and growth phenomena of semiconductor nanocrystals, by exploiting their size-dependent optical properties.[8,30] In particular, methods for obtaining quantitative data without perturbing the reaction both in microfluidic[33] and in flask synthesis[34] of semiconductor nanocrystals have been recently proposed. The UV-Vis spectrum of the solution was collected in situ by a dip probe apparatus, and the time dependence of the absorbance at 440 nm after co-injection is reported in Figure 4A. Following the injection, the absorbance exhibits a sharp peak and then for about 1 hour the absorbance does not undergo any significant variation; after that it suddenly increases over a few minutes quite rapidly and finally it gets too opaque to measure absorption.

Figure 4B shows the variation of the temperature after the injection (time=0) of the iron precursors and of the oxidizer, which is performed when the temperature of the solution is constant. As can be inferred, the injection induces a significant drop of the temperature, but after a few minutes the initial temperature of the solution recovers and no further temperature change is observed. In particular, no temperature variation is observed corresponding to the sudden increase of the absorbance recorded after about 1 hour from the injection.

The effect of iron precursor concentration on the reaction rate was studied by varying the initial amount of $Fe(CO)_5$, while keeping all other synthetic parameters constant. Figure 4C reports the dependence of the induction time (assumed as the time interval between injection and moment when the solution becomes dark) as a function of the iron molar concentration, showing that the reaction occurs much faster as the iron concentration is increased. As the precursor concentration is increased, smaller particle sizes are obtained.
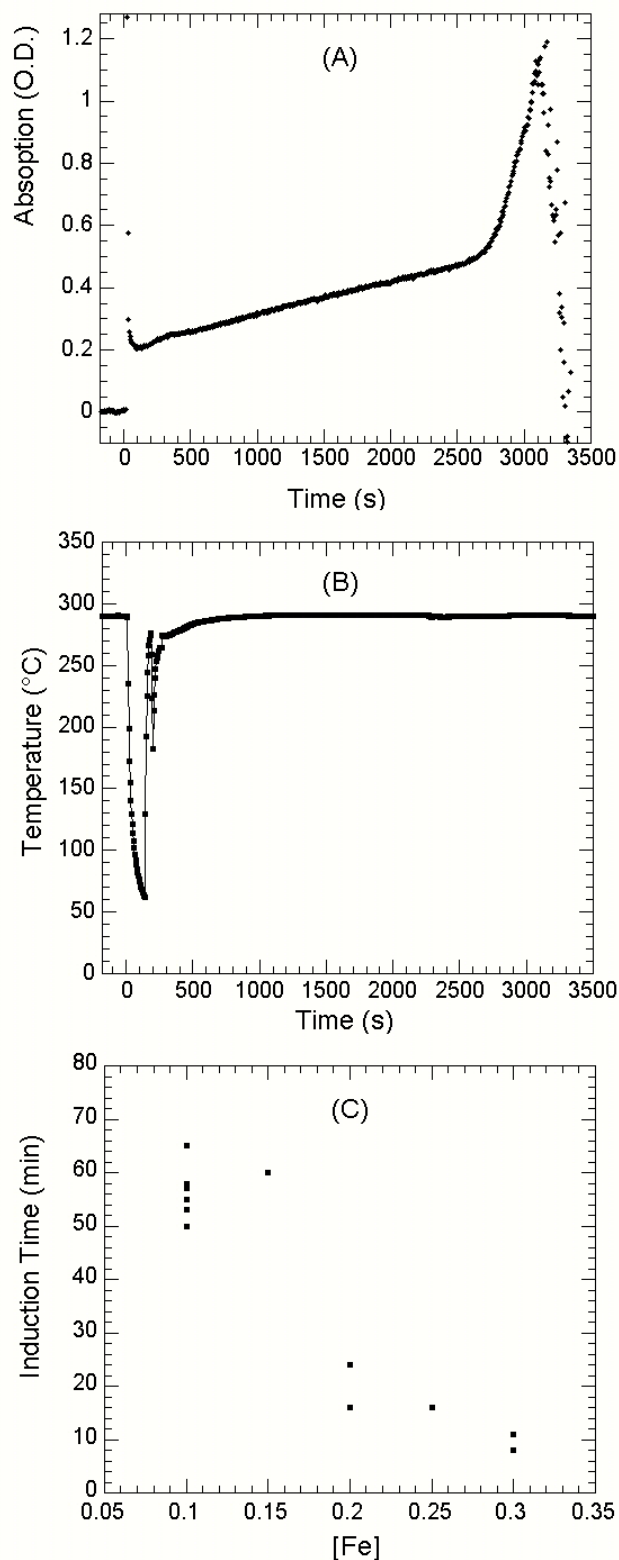
Figure 4. Optical density of the solution collected in situ at 440 nm during a typical synthesis carried out with molar ratios of Fe(CO)$_5$:mCPBA=1:1.5 (A) and corresponding temperature variation (B). The time=0 corresponds to the injection time; the induction time for particle formation under these conditions is about 1 hour. The dependence of the induction time on the iron precursor molar concentration is reported in (C).

Structural Characterization and Phase Control

Synthesis of single crystalline iron oxide nanocrystals Single crystalline nanocrystals were obtained by multiple injection of oxidizer experiments. In the typical synthesis, monodisperse nanoparticles were first formed by the reaction described previously, i.e. adopting a $Fe(CO)_5$: tridecanoic acid: mCPBA molar ratio of 1:3:1.5. One minute after the solution turns dark, an ether solution of mCPBA (mCPBA/ $Fe(CO)_5$ =1.5) was injected. Figure 5A shows the TEM images of the sample obtained by second injection of oxidizer: the sample is monodisperse with faceted particles of average diameter of 13 nm. The XRD spectrum, reported in Figure 5B, shows only the presence of a spinel phase, which could either correspond to the metastable phase of the ferric oxide γ-Fe_2O_3 (maghemite) or to the mixed valence iron II, III oxide Fe_3O_4 (magnetite). In fact, magnetite is an inverse spinel with ferrous ions in octahedral sites and ferric ions equally distributed between octahedral and tetrahedral sites. Maghemite is an inverse spinel that contains, as in magnetite, cations in tetrahedral and octahedral positions, but there are vacancies, usually in octahedral positions, to compensate for the increased positive charge. Although maghemite and magnetite have a slightly different cell parameter (8.351 Å for γ-Fe_2O_3 and 8.396 Å for Fe_3O_4),[35] due to the extra line broadening of the peaks the two nanocrystalline phases cannot be distinguished by X-Ray powder diffraction. Raman spectroscopy has been shown to be a powerful tool to investigate the structure of iron oxides and hydroxides.[29] In contrast to XRD, the Raman spectra of γ-Fe_2O_3 and Fe_3O_4 are sufficiently different and provide a means of distinguishing the two phases. Comparison of the Raman spectrum of the sample with reference materials indicates that the sample is a pure phase of γ-Fe_2O_3 (see Supplementary Information). In agreement, HR-TEM shown in Figure 5C indicates that the nanoparticles are single crystals with maghemite spinel structure.

As an alternative route, a large excess of oxidizer was used (iron pentacarbonyl:mCPBA molar ratio 1:4). In this case, XRD measurements show that only the spinel phase is formed, which was attributed from Raman spectroscopy to be Fe_3O_4. TEM observations, however, indicate the formation of nanoparticles with irregular shape and a broader size distribution (see Supplementary Information).
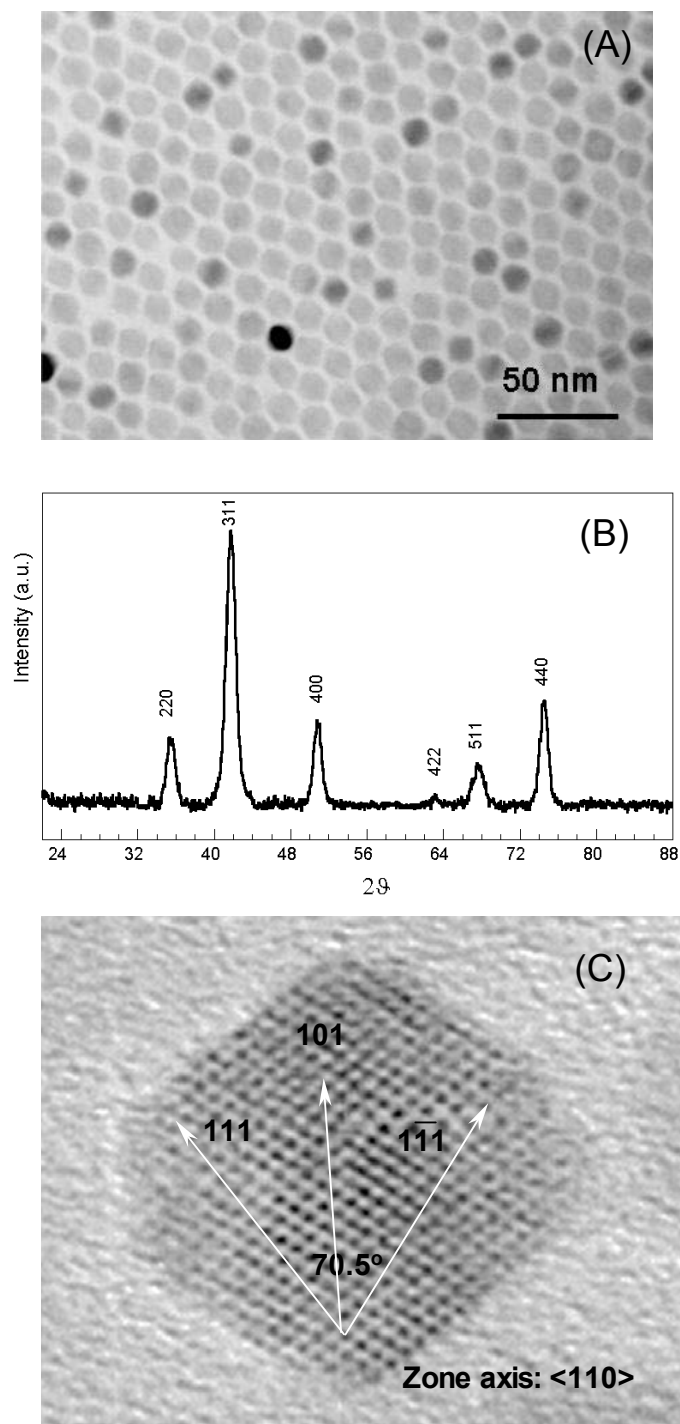
Figure 5. Low resolution TEM image (A), XRD spectrum (B), and high resolution TEM (C) of the sample obtained by performing sequential injections of oxidizer in order to obtain single crystalline spinel nanocrystals.

As-synthesized iron oxide nanocrystals The XRD spectrum of as-synthesized nanocrystals, shown in Figure 6a, cannot be attributed to only one polymorph of iron oxide. The XRD spectrum (see Figure 6b) of the aliquot corresponding to long growth time (1h 30') shows well resolved peaks that can be attributed to the presence of three phases: the ferrous oxide wüstite, a spinel phase plus a weak peak corresponding to the most intense peak of α-Fe. HRTEM results also support that the nanocrystals are mixed crystalline phase rather than single crystalline phase (see Supplementary Information).
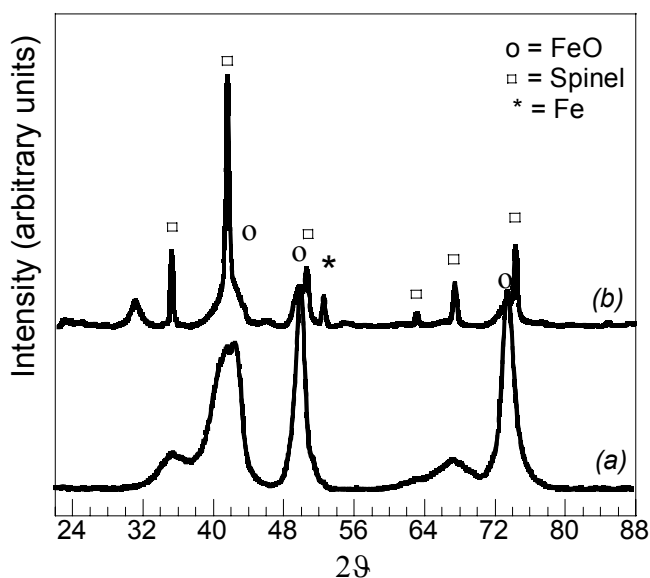

Figure 6. XRD spectra of the nanocrystals obtained by using a Fe(CO)$_5$:mCPBA=1:1.5 after a growth time of 5' (a) and 1h 30' (b). The radiation used is CoKα.

The Raman spectrum of our sample shows a total of three peaks at 662, 541, 314 cm^{-1}. Based on comparison to the bulk reference spectra (see Table I), the spinel phase can be therefore identified as Fe$_3$O$_4$. It is worth noting that the Raman spectrum of FeO is characterized by a single peak at 663 cm^{-1}, which is common to Fe$_3$O$_4$ as well.

Table I. Experimental position of Raman peaks for the sample and for reference iron oxides.

Sample (cm^{-1})	γ-Fe$_2$O$_3$ (cm^{-1})	Fe$_3$O$_4$ (cm^{-1})	FeO (cm^{-1})
662	700	663	663
541	504	533	
314	382	301	

Discussion

Pathway of formation of the nanocrystals

The iron oxide colloid formation is accompanied by a sudden change in the color of the reaction media from yellow to dark. The color variation, recorded by in situ UV-Vis spectroscopy, allows one to determine the induction time for particle formation. The induction time is strongly dependent on the precursor concentration, varying from one hour to ten minutes by increasing the iron concentration from 0.1 to 0.3 M, and indicates the presence of a delayed nucleation. Moreover, the colloid formation occurs through a burst-like reaction; this observation, together with the concentration dependence indicates the presence of a sudden supersaturation phenomenon. In agreement with this view, the concentration of the iron precursor affects the size of the resulting nanoparticles, and in particular smaller particles are obtained at higher iron concentrations. Moreover, both the UV-Vis data and the nanoparticle size evolution pattern determined by TEM analysis indicate that the growth rate is very fast. These results suggest that the formation of stable nuclei is considerably slower than their subsequent growth, so that the two phenomena are-as desired-temporally separated, and that the reaction rate is therefore controlled by the nucleation rate.

The origin of observed delayed nucleation was further investigated by decomposing the nanoparticle precursors under different conditions. When $Fe(CO)_5$ is decomposed under the same conditions reported above except for the absence of oxidizer, the formation of a dark colloid occurs with the same induction time measured for the preparation of the iron oxide nanoparticles. On the other hand, the thermal decomposition of $Fe(CO)_5$ in the presence of oxidizer without surfactant takes place in the time scale of less than 1 minute. These results indicate that the mCPBA does not play a determinant role in reaction kinetics. It has been reported that amines bind less strongly than carboxylic acids of the same carbon chain length.[36,37] We have therefore performed the decomposition of $Fe(CO)_5$ in the presence of dodecylamine as surfactant, recording an induction time of a few minutes.

It is noteworthy that $Fe(CO)_5$ may undergo condensation reactions to form higher nuclearity clusters, but in this case a progressive darkening of the solution should be observed as a consequence of the increasing metallic character of the bonding. For example, it is well-known that the photolysis of $Fe(CO)_5$ proceeds through clustering. In our case, however, the reaction kinetics is not affected by shining UV light on the solution during the reaction. In agreement with this view, Redl et al show by ex-situ IR spectroscopy that decarbonylation of $Fe(CO)_5$ readily occurs at temperatures above 170°C.[26]

All these observations can be summarized assuming that upon injection of the iron pentacarbonyl the iron is immediately coordinated and stabilized by the carboxylic acid present in solution. The metal-surfactant complex in turn is transformed into an "active species", which accumulates until it crosses the nucleation threshold. The higher the concentration of iron precursor, the shorter the retardation in nanocrystal nucleation.

In particular, when an $Fe(CO)_5$: tridecanoic acid: mCPBA ratio of 1:3:1.5 is adopted, the induction time is of about 1 hour and monodisperse nanocrystals of 13 nm in diameter are obtained. The delayed nucleation can be considered the key parameter in determining the monodispersity and the high reproducibility of the obtained nanoparticles, in that it allows the separation of the nucleation from the injection step and its related intrinsic uncertainies. In order to ensure size and shape control, a strict

control over all the reaction parameters is of particular importance when the synthesis is carried out under conditions far from equilibrium like the ones adopted here.

Size determination of iron oxide anisotropic nanocrystals

Several reports suggest that the monomer concentration can affect the shape of the particles. In this work, the shape of the nanoparticles was studied by the combined use of TEM and AFM. TEM is the most suitable technique for the determination of the particle diameter, but does not allow one to obtain straightforward information on the particle thickness. On the other hand, AFM gives accurate information on the height of the particles while it cannot give reliable estimates of the width of nanoparticles due to the convolution effect of the tip. AFM and TEM techniques can also be considered complementary techniques in sizing capped nanoparticles in that while the former gives information on the outer dimensions (i.e. including the surfactant coating), the latter affords images of the inorganic core.[38] Information on the surfactant coating can be obtained indirectly from TEM of close-packed monolayers, as the surfactant length dictates the distance between neighbouring particles. The average distance between nanoparticles in closed packed monolayers is 1.8 nm, giving an average surfactant length of 0.9 nm. The statistical analysis of AFM images of isolated particles having an inorganic core of 13 nm indicates a height of the capped nanoparticles of 3.16 nm. Banin and co-workers[39] pointed out that nanoparticle height can be underestimated by AFM in free air since the recorded height is the sum of the topography and the force gradient contributions. The latter contribution arises from the force gradient experienced by the tip when moving from the substrate to the sample, and is minimized when using a hydrophobic substrate (such as the graphite used in this case) whereas it is rather independent on the particle coating. In order to take into account the force gradient contribution we have analyzed aggregates made out of three layers, which have an average height h_a=14.66 nm. The force gradient experienced by the tip will be the same both in the case of the individual nanoparticles and of the assemblies, and we can therefore assume that both height determinations will be affected by the same error. By subtracting the height of the isolated nanoparticles h_i, one can therefore remove the force

gradient contribution from the height of the 3-layer aggregate (h_a), obtaining therefore the height of 2 layers. From this analysis, we derive a value of a capped nanoparticle of 5.75 nm, and taking into account the contribution of the surfactant coating the resulting height of the nanoparticle is 3.95 nm. The aspect ratio larger than 3 resulting from the combined analysis of TEM and AFM data indicate the formation of the particles in an anisotropic growth regime, which can be induced by the high monomer concentration[11,30] arising both from the high concentration of the precursors and the strong supersaturation following the delayed nucleation.

Crystal Structure and Phase Control

XRD and HR-TEM data of the sample prepared by using a $Fe(CO)_5$:mCPBA molar ratio of 1:1.5 (reported in Figure 5 and in the Supplementary Information, respectively) indicate that the particles are polycrystalline. At early growth times, wüstite and magnetite phases are present. Wüstite is the Fe(II) oxide; however, this phase is typically non-stoichiometric with formula $Fe_{1-x}O$ (x ranging from .05 to .17), where the iron deficiency is compensated by partial oxidation of Fe^{2+} ions to Fe^{3+}. Although stable at high temperature and pressure, wüstite can be obtained as metastable phase in rapidly quenched samples.[36] The presence of wüstite and magnetite domains in the nanoparticles can be understood considering the compatibility of the two oxides both from the compositional and structural point of view. In fact, not only defect clusters present in wüstite approach the Fe_3O_4 structure, but both the FeO structure (rock salt-type) and the spinel Fe_3O_4 are based on a cubic close packed oxygen lattice, where the oxygen layers are cubic close packed along the (111) axis. For example, the formation of biphase ordered Fe_3O_4 (111) defect structures with FeO(111) domains has been recently extensively characterized by LEED, STM, and Auger spectroscopy.[35] Colloidal nanoparticles obtained by the decomposition of $Fe(CO)_5$ in the presence of pyridine N-oxide as oxidizer mainly composed of the wustite phase with small seeds of magnetite[26] were also reported, whereas under inert conditions low crystallinity wustite and maghemite domains were obtained.[40] In the sample obtained at longer growth time the XRD data indicate a peak sharpening due to the crystal growth, and that bcc-Fe is present

together with wüstite and magnetite, the latter being the main phase. This result indicates that, in agreement with the phase diagram,[37] wüstite undergoes dismutation giving rise to Fe and Fe_3O_4.

It is noteworthy that a complete oxidation of iron would be expected when using a $Fe(CO)_5$:mCPBA molar ratio of 1:1.5, whereas FeO and Fe_3O_4 are formed indicating the presence of a mixture of Fe(II,III). By using a large excess of mCPBA ($Fe(CO)_5$:mCPBA=1:4) Fe_3O_4 nanocrystals are obtained, as a consequence of a higher but still incomplete oxidation of iron. These observations suggest that the decomposition of the oxidizer is fast compared to the decomposition of the iron pentacarbonyl. In agreement with this picture, the sequential injection of oxidizer is more effective than the use of an initial excess of oxidizer. By using the same initial conditions ($Fe(CO)_5$: tridecanoic acid: mCPBA = 1:3:1.5) and then injecting a second amount of mCPBA so that the overall nominal iron-to-oxidizer molar ratio is 1:3, the ferric oxide γ-Fe_2O_3 was indeed obtained. When a small amount of mCPBA is sequentially injected so that the overall nominal iron-to-oxidizer molar ratio is 1:2, the mixed valence spinel oxide Fe_3O_4 is obtained. The second injection of oxidizer does not alter the shape and size of the nanoparticles before the injection, likely due to the ease of interconversion between these structures. Similarly, it has been reported that the morphology of parent wustite nanocrystals does not change after phase transition to magnetite obtained by annealing at 400°C under inert atmosphere.[26]

Effect of the Temperature on the size of the nanoparticles.

On the other hand, the size of the initial nanoparticles is strongly affected by factors such as the precursor concentration and the reaction temperature. In particular, if the reaction is carried at 280°C and at 285°C polydisperse nanocrystals with average diameter of 14 nm and 35 nm respectively are obtained, whereas if the reaction is performed at 298°C the resulting nanoparticles are monodisperse and have an average diameter of 7 nm. As mentioned earlier, an increase in the iron concentration leads to smaller particles: monodisperse nanocrystals with average diameter of 7 nm are obtained by doubling the iron pentacarbonyl concentration. These observations are in agreement with the proposed

mechanism, as both a higher temperature and a larger iron concentration will speed up the reaction and induce the formation of smaller nuclei.
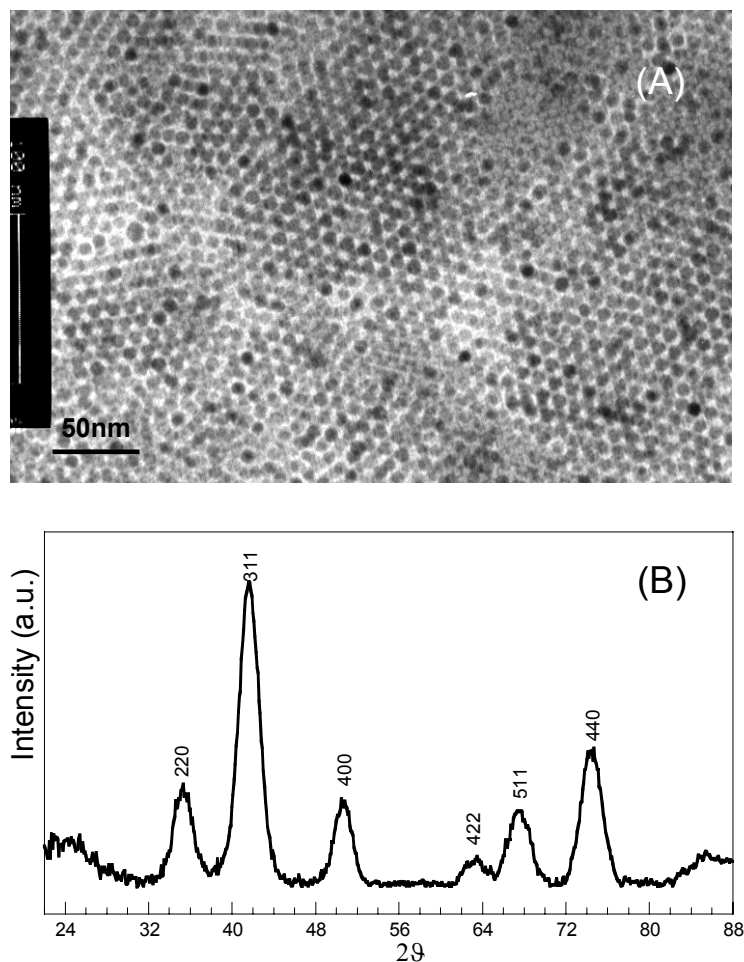

Figure 7. Low resolution TEM image (A), and XRD spectrum (B) of the sample obtained by carrying the synthesis at higher temperature followed by a 2nd injection of oxidizer.

Since multiple injections of oxidizer do not alter the size distribution of the nanoparticles once they are formed, iron oxide spinel single crystals with a controlled size can be obtained by adopting suitable initial conditions followed by a 2nd injection. The sequential injection of oxidizer on nanoparticles grown at 298°C using an overall iron-to-oxidizer ratio of 1:3 (the same conditions adopted for the sample reported in Fig.6 except for the temperature that in this case is 5 °C higher), leads to monodisperse nanoparticles having diameter of 7 nm (Figure 7A). The XRD data, reported in Fig. 7B,

indicate the presence of a single spinel phase, and the peak broadening confirms that the particles are smaller than in the sample reported in Fig.6B.

Conclusions

The pyrolysis of the suitable organometallic precursor and of an oxidizer in the presence of a coordinating surfactant is used to form nanocrystals with defined size and phase of a complex system such as iron oxide. The formation of the colloid, which is accompanied by a color change, is monitored by in situ UV-Vis spectroscopy which points out the presence of a delayed nucleation process and provides a means of measuring the induction time. The effect of the different synthesis parameters on the formation mechanism suggest that the retardation of the nucleation is induced by the fatty acid used as coordinating surfactant, which strongly stabilizes the monomer in solution. The delayed nucleation results in a very pronounced monomer supersaturation peak after the induction time. As a consequence, the presence of monodisperse nuclei and a fast growth regime are responsible for the formation of nanocrystals with nearly monodisperse size and anisotropic shape, respectively. Under the adopted conditions, the decomposition of the oxidizer is faster than that of the iron precursor, so that the most effective method to obtain iron oxide nanocrystals with the desired oxidation state is the sequential injection of oxidizer at different stages of decomposition of the iron precursor. The delayed nucleation mechanism results in the occurrence of nanoparticle crystallization well separated in time from the injection of the precursors. Procedures involving a delayed nucleation can be achieved by using suitable strongly coordinating surfactants and are expected to improve the reproducibility and ease of scale-up of colloidal nanocrystals.

22

Supporting Information Available

Statistical Analysis of AFM data to obtain the height of the nanoparticles; Additional TEM and HRTEM of the polycrystalline sample; Raman spectrum of the single crystalline γ-Fe_2O_3 sample; XRD and TEM of the sample obtained with an excess of oxidizer.

REFERENCES

1. Alivisatos, A. P. *Science* **1996**, 271, 933.

2. Fine Particles. Synthesis, Characterization and Mechanism of Growth, Tadao Sugimoto, editor, Marcel Dekker , Inc. NY 2000.

3. Tang, J.; Fabbri, J.; Robinson, R.D.; Zhu, Y.; Herman, I.P.; Steigerwald, M.L.; Brus, L.E. *Chem. Mater.* **2004**, *16*, 1336.

4. Yin, M.; O'Brien, S.; *J. Am. Chem. Soc.;* **2003**; *125*; 10180.

5. Borchert, H.; Shevchenko, E. V.; Robert, A.; Mekis, I.; Kornowski, A.; Grubel, G.; Weller, H. *Langmuir* **2005**; *21*; 1931.

6. Yu, W. W.; Falkner, J. C.; Shih, B. S.; Colvin, V. L. *Chem. Mater.***; 2004**; *16*; 3318.

7. Murray C.B., Norris,D.J., Bawendi, M.G. *J. Amer. Chem. Soc.* **1993**, *115, 8706.*

8. Manna, L., Scher, E. C., Alivisatos, A.P. *J. Amer. Chem. Soc.* **2000,** *122*, 12700

9. Zaziski, D., Prilliman, S., Scher, E., Casula, M., Wickham, J.,. Clark, S. M., Alivisatos, A. P. *NanoLett*., **2004**, *4* , 943.

10. Ramaswamy, V.; Haynes, T. E.; White, C. W.; MoberlyChan, W. J.; Roorda, S.; Aziz, M. J. *Nano Lett.* **2005**; *5*; 373.

11. Jun, Y-w; Casula, M. F.; Sim, J-W; Kim, S. Y.; Cheon, J.; Alivisatos, A. P. *J. Am. Chem. Soc.,* **2003**, *125,* 15981.

12. Lee, S.-M.; Jun, Y.; Cho, S.-N.; Cheon, J. *J. Am. Chem. Soc.* **2002**, *124*, 11244.

13. Alivisatos, A.P. et al., Nature, in press.

14. Dormann, J.; Fiorani, D. Magnetic Properties of Fine Particles, North Holland, Amsterdam, The Netherlands, 1992.

15. Banfield, J.F.; Welch, S.A.; Zhang, H. Z.; Ebert TT.; Penn, R.L. *Science* **2000***, 289,* 751.

16. Li, S.; Meitzner, G. D. ; Iglesia, E. *J. Phys. Chem. B* **2001**, *105*, 5743.

17. Tartaj, P.; Morales, M. P.; Veintemillas-Verdaguer, S.; Gonzales-Carreno, T.; Serna, C.J. *J. Phys. D: Appl. Phys.* **2003**, *36*, R182.

18. Gash, A. E.; Tillotson, T.M.; Satcher, J.H.; Poco, J.F.; Hrubesh, L.W.; and Simpson, R.L. *Chem. Mater.* **2001**, *13*, 999.

19. Prakash, A.; McCormick, AV.; Zachariah MR. *Chem. Mater.* **2004**, *16*, 1466.

20. Cornell, R.M.; Schwertmann, U. *The Iron Oxides. Structure, Properties, Reactions, Occurrence and Uses*, VCH, Weinheim, Germany, 1996.

21. Rockenberger, J.; Scher, E.; Alivisatos, A.P. *J .Am.Chem. Soc.* **1999**, *121*, 11595.

22. Sun, S.; Zeng, H. *J. Am. Chem. Soc.* **2002**, *124*, 8204.

23. Sun, S.; Zeng, H.; Robinson, D. B.; Raoux, S.; Rice, P. M.; Wang, S. X.; Li, G. J. Am. Chem. Soc. **2004**, *126*, 273.,

24. Park, J.; An, K.; Hwang, y.; Park, J.-G.; Noh, H.-J.; Kim, J.-Y.; Park, J.-H.; Hwang, N.-M.; Hyeon, T. Nat.Mater. **2004**, *3*, 891.

25. Jana, N. R.; Chen, Y.; Peng, X. Chem. Mater. **2004**, *16*, 3931

26. Redl, F.X.; Black, C.T.; Papaefthymiou, G.C.; Sandstrom, R.L.; Yin, M.; Zeng, H.; Murray, C.B.; O'Brien, S.P. *J. Am. Chem. Soc.* **2004**, *126*, 14583.

27. Cheon, J.; Kang, N-J.; Lee, S-M.; Lee, J-H.; Yoon, J-H.; Oh, S. J. *J. Am. Chem. Soc.* **2004**, *126*, 1950.

28. Hyeon, T.; Lee S.S.; Park, J.; Chung, Y.; Na, H.B. *J. Am. Chem. Soc.* **2001**, *123*, 12798.

29. de Faria, D.L.; Venancio Silva, S.; de Oliveira, M.T. *J. Raman Spectrosc.* **1997**, *28*, 873.

30. Peng, Z.A.; Peng, X. *J. Am. Chem. Soc.* **2002**, *124*, 3343.

31. Dante S.; Hou, Z.; Risbud, S.; Stroeve, P. *Langmuir* **1999**, *15*, 2176.

32. Bentzon, M.D.; van Wonterghem, J.; Morup, S.; Tholen, A.; Koch, C.J.W., *Philos.Mag. B* **1989**, *60*, 169.

33. Chan, E.; Mathies, R.A.; Alivisatos A.P. *Nano Lett.* **2003**, *3*, 199.

34. Qu, L.; Yu, W.W.; Peng, X. *Nano Lett* **2004**, *4,* 465.

35. Ketteler, G.; Weiss, W.; Ranke, W.; Schlogl, R. *PhysChemChemPhys* **2001**, *3*, 1114

36. Li, Y.; Liu, J.; Wang, Y.; Wang, Z.L. *Chem. Mater.* **2001**, *13*, 1008

37. Blums, E.; Cebers, A.; Maiorov, M.M. *Magnetic Fluids,* 1997, De Gruyter, Berlin

38. Reetz, M.T.; Helbig, W.; Quaiser, S.A.; Stimming, U.; Breuer, N.; Vogel, R. *Science* **1995**, *267*, 367.

39. Ebenstein, Y.; Nahum, E.; Banin, U. *NanoLett* **2002**, *2*, 945.

40. Woo, K.; Hong, J.; Choi, S.; Lee, H-W.; Ahn, J-P.; Kim, C. S.; Lee, S.W. *Chem. Mater.* **2004**, *16*, 2814.

Table of Contents graphic: